

Numerical study on the dynamics of primary cilium in pulsatile flows by the immersed boundary-lattice Boltzmann method

Jingyu Cui¹, Yang Liu^{1*}, Bingmei M. Fu²

¹Department of Mechanical Engineering, The Hong Kong Polytechnic University, Hung Hom, Hong Kong

²Department of Biomedical Engineering, City College of New York, USA

Abstract

An explicit immersed boundary-lattice Boltzmann method is applied to numerically investigate the dynamics of primary cilium in pulsatile blood flows with two-way fluid-structure interaction considered. To well characterize the effect of cilium basal body on cilium dynamics, the cilium base is modeled as a nonlinear rotational spring attached to the cilium's basal end as proposed by Resnick (2015). After several careful validations, the fluid-cilium interaction system is investigated in detail at various pulsatile flow conditions which are characterized by peak Reynolds numbers (Re_{peak}) and Womersley numbers (Wo). The periodic flapping of primary cilium observed in our simulations is very similar to the *in vivo* ciliary oscillation captured by O'Connor et al. (2013). The cilium's dynamics is found to be closely related to the Re_{peak} and Wo . Increase the Re_{peak} or decrease the Wo brings to an increase in the cilium's flapping amplitude, tip angular speed, basal rotation and maximum tensile stress. It is also demonstrated that by reducing the Re_{peak} or enhancing the Wo to a certain level, one can shift the flapping pattern of cilium from its original two-side one to a one-side one, making the stretch only happen on one particular side. During the flapping process, the location of the

maximum tensile stress is not always found at the basal region, instead, it is able to propagate from time to time within a certain distance to the base. Due to the obstruction of the primary cilium, the distribution of wall shear stress no longer remains uniform as in the absence of cilia. It oscillates in space with the minimum magnitude always found near where the cilium is located. The presence of cilium also reduces the overall level of wall shear stress, especially at the region near the cilium's anchor point.

Keywords: Immersed boundary, lattice Boltzmann method, primary cilium, fluid-structure interaction, pulsatile flow

1 Introduction

Primary cilia are filament-like, immotile organelles solitarily protruding into extracellular space from the apical surface of nearly every mammalian cell, like antennas (Hagiwara et al. 2008; Nguyen and Jacobs 2013). Though primary cilia were originally discovered over a century ago, their exact functions remain to be incompletely understood. Compared with the better-understood motile cilium, the primary cilium possesses a similar but relatively simpler structure. As shown in Fig. 1, though both of these two cilium kinds have a membrane-enclosed axoneme which contains nine circumferentially arranged doublet microtubules, there is no additional central pair appearing at the axoneme of primary cilium, resulting in a “9+0” arrangement. The primary cilium also lacks other axonemal components that appear in motile cilium, including radial spokes, dynein arms, and nexin links, thus cannot spontaneously generate internal forces (Resnick 2015).

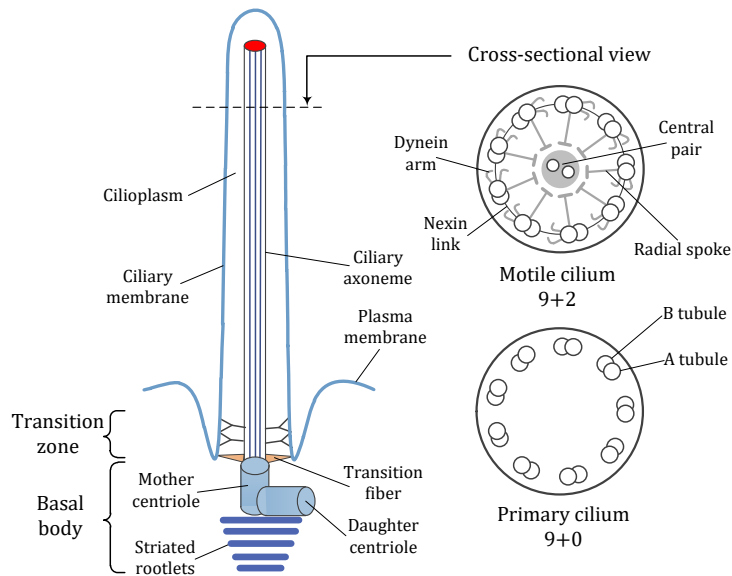


Fig. 1 Sketch of structures of primary cilium and motile cilium

Though being long considered as vestigial structures, the primary cilia are recently demonstrated to play a crucial role in vertebrate development and inherited human diseases (Goetz and Anderson 2010). On the other hand, proper function and homeostasis of a wide range of cells and tissues require mechanical stimuli from the extracellular environment. Variation of these stimuli, such as the oscillation of the fluid flow, changes of osmolality due to transmembrane salt and water transport, and hydrostatic pressure increase in renal tubule flow, needs to be sensed and transduced among different cell components. Recent studies have revealed that the primary cilium acts as a sensor for those mechanical stimuli, as it has been observed by experiments that the passively bending behavior of primary cilia is correlated with the initiation of a variety of signaling cascades (Nauli et al. 2003; Praetorius et al. 2003; Praetorius and Spring 2001; Praetorius and Spring 2003). For instance, in ciliated kidney cells,

the deflection of an epithelial primary cilium by a fluid flow or micropipette elicits an increased level of intracellular calcium, an important second messenger communicating the extracellular activities with the cell nucleus. In contrast to ciliated cells, kidney cells without cilia are unable to translate the mechanical stimulation into the cell nucleus by increasing intracellular calcium levels. This deflection-triggered calcium increase, to be more specific, relies on the opening of the PC2 cation channel which is responsible for calcium ion influx. This PC2 cation channel is localized to the primary cilia and is assumed to be stretch-activated (Praetorius and Spring 2001; Praetorius and Spring 2003). The resulting change in the intracellular calcium concentration then regulates numerous molecular activities inside the cell that contribute to tissue and organ development (Nauli et al. 2003). A similar mechanism has also been found in blood-pressure maintenance in the vasculature, where the vessel diameter is regulated by endothelial primary cilia through adjusting nitric oxide production (Boo and Jo 2003; Nauli et al. 2008). So far, little is known about the mechanical mechanism behind this deflection-triggered opening of signaling pathways. For example, what are the possible flow-induced bending behaviors of primary cilia and how to interpret them? What is the threshold value of stretch/deflection for activating a corresponding signaling pathway? These all remain to be answered. Elucidating this mechanism needs a combination of experimental and numerical approaches, as the force and stress distribution on cilium along with other mechanical properties are still beyond the capability of experimental approaches due to the scales of the quantities involved. By using numerical approaches, much more detailed dynamic information can be obtained.

In addition, defects of primary cilium in ciliary protein or its physical structure are linked with numerous diseases known as ciliopathies, for instance, polycystic kidney disease (Yoder

2007; Yoder et al. 2002), cystic and fibrotic liver disease (Masyuk et al. 2008), osteoarthritis (McGlashan et al. 2008), obesity (Sen Gupta et al. 2009) and even cancer (Hassounah et al. 2012; Menzl et al. 2014). So one potential approach for treating those ciliopathies is to rescue or regulate the affected cilium form and its mechanosensing function. It has already been suggested that through adjusting the parameters of primary cilia, e.g., the length and bending module, one can alter the deflection response of cilium to mechanical stimuli, and further manage to manipulate the mechanosensitivity of primary cilia (Khayyeri et al. 2015). Recently, an experiment aimed to alter the bending modulus of primary cilia via pharmacological treatment was successfully performed (Resnick 2016). Other approaches such as using a magnetic force to manipulate the dynamics of artificial cilia to generate a directional local flow were also reported (Hanasoge et al. 2018). Therefore, conducting numerical studies on the fluid-cilium interaction system will enrich our understanding of ciliopathies and help explore its potential treatments.

Several models have been developed to study cilium deflection. The simplest one is the homogeneous cantilevered Euler-Bernoulli beam model, which has been used extensively to determine the mechanical properties of primary cilia under static load. Schwart et al. (1997) firstly used this model to evaluate the flexural rigidity of primary cilium based on an imaged-informed approach. By assuming a constant flow velocity distribution along the cilium length, the Euler-Bernoulli equation was solved using both quadruple integration model and heavy elastic model, and the final bending profile of the cilium was obtained. The flexural rigidity was then iteratively updated during each calculation until the predicted bending shape matched the experimentally observed deflection. Following their steps, this model was further developed

to account for the initial cilium shape and basal rotation (Downs et al. 2014), in combination with a more realistic flow velocity profile (Liu et al. 2005). However, experimental observations have been reported to deviate from this cantilevered Euler-Bernoulli beam model (Downs et al. 2014; Nguyen et al. 2015; Resnick 2015). Moreover, Young et al. (2012) studied the cilium dynamics in shear flow using slender body theory, in which the effect of the basal body is incorporated as a damped rotational spring and a good agreement between experimental measurements and numerical calculations was obtained. Modeling the cilium base as a rotational spring has further been proved to match experimentally measured resonant oscillation of primary cilia and was believed to be more physically meaningful in Resnick's work, in which the linear and nonlinear spring constants for modeling cilium basal body are determined based on an optical trap technique (Resnick 2015). Khayyeri et al. (2015) developed a 3-dimensional finite element model for the whole cell-cilium system, in which the cell components are separately modeled. However, in most studies that used computational analysis, the flow conditions are simplified to either static Stokes flow or shear flow in order to easily evaluate the hydrodynamic load, which fails to reveal the transient and oscillatory nature of many biological flows, for instance, the blood flow and the renal tubule flow. Apart from that, the effect of cilia on the fluid flow is usually ignored in those models, which is assuredly another contributing factor for determining cilium dynamics.

In this paper, we introduce an explicit immersed boundary-lattice Boltzmann method (IB-LBM) for studying the dynamics of primary cilia in pulsatile flows with two-way fluid-structure interaction considered. The method is easy to implement and robust in handling moving elastic boundaries. After some careful validations, this fluid-cilium interaction system is investigated

in detail with the effect of cilium basal body incorporated as a nonlinear rotational spring.

2 Mathematical formulation and numerical method

2.1 Flow solver

The governing equations of two-dimensional incompressible viscous flow with external force can be expressed as

$$\rho \left(\frac{\partial \mathbf{u}}{\partial t} + \mathbf{u} \cdot \nabla \mathbf{u} \right) = -\nabla p + \mu \Delta \mathbf{u} + \mathbf{f} \quad (1)$$

$$\nabla \cdot \mathbf{u} = 0 \quad (2)$$

where $\mathbf{u} = (u, v)$ is the fluid velocity, ρ and μ the density and dynamic viscosity of the fluid, respectively. p is the pressure and \mathbf{f} the external force from the immersed structural boundary.

Equations (1) and (2) can be solved by lattice Boltzmann method (LBM). In present simulations, a single-relaxation-time based LBM with a D2Q9 lattice model is adopted. The dimensionless form of LBM under an external force is given by Guo et al. (2002) as follows,

$$f_j(\mathbf{x} + \mathbf{e}_j \Delta t, t + \Delta t) - f_j(\mathbf{x}, t) = -\frac{1}{\tau} (f_j(\mathbf{x}, t) - f_j^{eq}(\mathbf{x}, t)) + \mathbf{F}_j \Delta t \quad (3)$$

With the force term \mathbf{F}_j being

$$\mathbf{F}_j = \left(1 - \frac{1}{2\tau} \right) \omega_j \left(\frac{\mathbf{e}_j \cdot \mathbf{u}}{c_s^2} + \frac{\mathbf{e}_j \cdot \mathbf{u}}{c_s^4} \mathbf{e}_j \right) \mathbf{f}(\mathbf{x}, t) \quad (4)$$

where $j = 0, 1, \dots, 8$ denotes the lattice space, $f_j(\mathbf{x}, t)$ is the density distribution function of particles whose position vector is \mathbf{x} at time t . τ is the dimensionless relaxation time which is related to the dimensionless kinematic viscosity ν and sound speed c_s by $\nu = c_s^2(\tau - 0.5)\Delta t$. Here Δt is the time interval and $c_s = 1/\sqrt{3}$. $f_j^{eq}(\mathbf{x}, t)$ is the Maxwellian equilibrium distribution function which takes the following form under the BGK approximation.

$$f_j^{eq}(\mathbf{x}, t) = \omega_j \rho \left[1 + \frac{\mathbf{e}_j \cdot \mathbf{u}}{c_s^2} + \frac{(\mathbf{e}_j \cdot \mathbf{u})^2}{2c_s^4} - \frac{\mathbf{u}^2}{2c_s^2} \right] \quad (5)$$

where ω_j is the weights coefficient corresponding to the chosen velocity model, whose value

takes: $\omega_0 = 4/9$, $\omega_{1,2,3,4} = 1/9$ and $\omega_{5,6,7,8} = 1/36$. \mathbf{e}_j is the lattice velocity set which is given as

$$\mathbf{e}_j = \begin{cases} (0, 0), & j = 0 \\ c \left(\cos \frac{\pi(j-1)}{2}, \sin \frac{\pi(j-1)}{2} \right), & j = 1, 2, 3, 4 \\ \sqrt{2}c \left(\cos \frac{\pi(2j-1)}{4}, \sin \frac{\pi(2j-1)}{4} \right), & j = 5, 6, 7, 8 \end{cases} \quad (6)$$

where c is the lattice speed, whose value is $c = \Delta x / \Delta t = 1$, with Δx being the lattice space.

Finally, the macroscopic fluid density ρ and velocity \mathbf{u} can be recovered by:

$$\rho = \sum_j f_j, \quad \rho \mathbf{u} = \sum_j f_j \mathbf{e}_j + \frac{1}{2} \mathbf{f} \Delta t \quad (7)$$

2.2 Structure solver

The motion equation for a filament-like structure under hydrodynamic load is given by

(Connell and Yue 2007; Zhu and Peskin 2003)

$$\rho_c \frac{\partial^2 \mathbf{X}}{\partial t^2} = \frac{\partial}{\partial s} \left[T(s) \frac{\partial \mathbf{X}}{\partial s} \right] - K_b \frac{\partial^4 \mathbf{X}}{\partial s^4} + \mathbf{F}_{fluid} \quad (8)$$

where $\frac{\partial}{\partial s} \left[T(s) \frac{\partial \mathbf{X}}{\partial s} \right]$ and $-K_b \frac{\partial^4 \mathbf{X}}{\partial s^4}$ are the internal stretching and bending forces of the structure, respectively. \mathbf{F}_{fluid} is the hydrodynamic force exerting on the structure from its ambient fluid, and $T(s)$ the tensile force which can be expressed as

$$T(s) = K_s \left(\left(\frac{\partial \mathbf{X}}{\partial s} \cdot \frac{\partial \mathbf{X}}{\partial s} \right)^{\frac{1}{2}} - 1 \right) \quad (9)$$

Here \mathbf{X} is the position vector of the structure point, s the Lagrangian coordinate along the length. The linear density ρ_c , stretching coefficient K_s and bending rigidity K_b are 3 constants decided by the intrinsic properties of the structure.

In our simulations, the primary cilium is equally divided into segments by a set of isometric Lagrangian point $\mathbf{X}(s_i, t)$, $i = 0, 1, \dots, Nb$. The stretching and bending forces are calculated explicitly using a finite difference method.

$$\frac{\partial}{\partial s} \left[T(s) \frac{\partial \mathbf{X}}{\partial s} \right] = \frac{T_{i+\frac{1}{2}} \left[\frac{\partial \mathbf{X}}{\partial s} \right]_{i+\frac{1}{2}} - T_{i-\frac{1}{2}} \left[\frac{\partial \mathbf{X}}{\partial s} \right]_{i-\frac{1}{2}}}{\Delta s} \quad (10)$$

$$-K_b \frac{\partial^4 \mathbf{X}}{\partial s^4} = -K_b \frac{\mathbf{X}_{i+2} - 4\mathbf{X}_{i+1} + 6\mathbf{X}_i - 4\mathbf{X}_{i-1} + \mathbf{X}_{i-2}}{\Delta s^4} \quad (11)$$

with $\partial \mathbf{X} / \partial s$ being the tangent vector and Δs the Lagrangian grid spacing. The tension force $T_{i+\frac{1}{2}}$ is calculated using Hooke's law.

$$T_{i+\frac{1}{2}} = K_s \left(\left| \frac{\mathbf{X}_{i+1} - \mathbf{X}_i}{\Delta s} \right| - 1 \right), \text{ and } T_{i-\frac{1}{2}} = K_s \left(\left| \frac{\mathbf{X}_i - \mathbf{X}_{i-1}}{\Delta s} \right| - 1 \right) \quad (12)$$

The boundary position \mathbf{X}_i and velocity \mathbf{U}_i are updated using the Velocity Verlet method.

$$\mathbf{X}_i^{n+1} = \mathbf{X}_i^n + \Delta t \mathbf{U}_i^n + \frac{1}{2} \mathbf{a}_i^n (\Delta t)^2 \quad (13)$$

$$\mathbf{U}_i^{n+1} = \mathbf{U}_i^n + \frac{\Delta t}{2} (\mathbf{a}_i^n + \mathbf{a}_i^{n+1}) \quad (14)$$

where \mathbf{a} is the acceleration, i.e. $\partial^2 \mathbf{X} / \partial t^2$ which is calculated by Equation (8). The superscript n is the time step index and subscript i represents the i th boundary point.

2.3 Fluid-structure interaction

The fluid-structure interaction (FSI) between the flow and primary cilium is solved by a momentum exchange scheme-based immerse boundary method (IBM) (Niu et al. 2006), which is slightly different from the original one proposed by Peskin (2003). In this method, the distribution functions of the boundary points need to be interpolated. One efficient way to do this is using the smoothed Dirac delta function $\sigma_h(\cdot)$ (Yuan et al. 2014),

$$f_j(\mathbf{X}, t) = \sum_{\mathbf{x}} f_j(\mathbf{x}, t) \sigma_h(\mathbf{x} - \mathbf{X}) \Delta x^2 \quad (15)$$

where Δx is the Eulerian grid spacing and $\sum_{\mathbf{x}}$ denotes the summations over all Eulerian grids.

To satisfy the no-slip boundary condition on the fluid-structure interface, a new set of boundary distribution functions is computed using the bounce-back rules (Ladd 1994a; Ladd

1994b).

$$f_{-j}(\mathbf{X}, t + \Delta t) = f_j(\mathbf{X}, t) - 2\omega_j \rho \frac{\mathbf{e}_j \mathbf{U}(\mathbf{X}, t)}{c_s^2} \quad (16)$$

where $-j$ denotes the opposite direction of j , i.e. $\mathbf{e}_{-j} = -\mathbf{e}_j$ and $\mathbf{U}(\mathbf{X}, t)$ is the velocity of the boundary points. Consequently, the hydrodynamic force density on the structural boundary $\mathbf{F}_{fluid}(\mathbf{X}, t)$ can be computed via momentum exchange method as bellow,

$$\mathbf{F}_{fluid}(\mathbf{X}, t) = -\mathbf{f}_e(\mathbf{X}, t) = -\sum_j \mathbf{e}_j [f_j(\mathbf{X}, t + \Delta t) - f_{-j}(\mathbf{X}, t)] \quad (17)$$

The reaction force of $\mathbf{F}_{fluid}(\mathbf{X}, t)$ is further transformed into a body force distributing to its surrounding fluid,

$$\mathbf{f}_e(\mathbf{x}, t) = -\sum_{\mathbf{X}} \mathbf{F}_{fluid}(\mathbf{X}, t) \sigma_h(\mathbf{x} - \mathbf{X}) \Delta s \quad (18)$$

where $\sum_{\mathbf{X}}$ denotes the summations over all the Lagrangian grid points.

2.4 Model the cilium basal body

Previous cantilevered beam model is proved to be incorrect for modeling cilium deflection, as the cilium basal body could experience some degrees of rotation rather than remain clamped when subject to a fluid flow (Downs et al. 2014; Nguyen et al. 2015; Resnick 2015). Here we follow the approach of Resnick (2015) by modeling the cilium basal body as a nonlinear rotational spring (see Fig. 2). Every basal rotation induced by the fluid drag will generate a reverse bending moment at the basal end due to the spring. Similar treatment has also been used by Young et al. (2012) and the results are proved to match experimental observations.

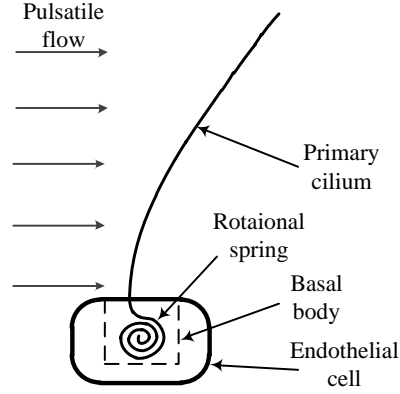


Fig. 2 The nonlinear rotational spring model for modeling the basal body of a primary cilium

3 Numerical validation

3.1 Planar Poiseuille flow

The validity of the present flow solver is verified by simulating a 2-dimensional planar Poiseuille flow, a simple and well-documented test case with the analytical solution given as,

$$u(y) = \frac{\Delta P}{2L\rho\nu} (Dy - y^2) \quad (19)$$

where D and L is the width and length of the channel, respectively. ρ is the density and ν the kinetic viscosity of the fluid. $\Delta P/L$ is the pressure gradient along the x -direction.

In our simulation, a body force density f_d is applied to the fluid nodes as a substitution of the pressure gradient to produce a driven flow. This trick has been widely adopted in the LBM community to simulate Poiseuille flows, as in references (Kruger et al. 2014; O'Connor et al. 2016). The applied body force density is equivalent to a pressure gradient under the relation of

$$\frac{\Delta P}{L} = f_d \quad (20)$$

The present simulation domain is a square with a uniform mesh size of 80×240 at

Reynolds number $Re = 50$. The periodic boundary condition is used in the flow direction and a no-slip boundary condition imposed on walls. As shown in Fig. 3, our simulation result coincides well with the analytical solution.

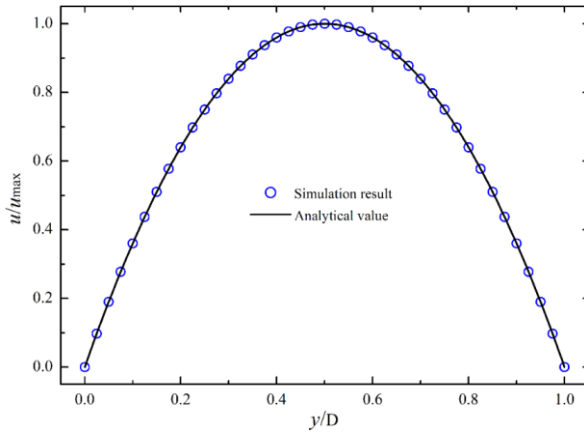


Fig. 3 Comparison of the simulation result and the analytical solution

3.2 Rope pendulum swinging under gravity

The swinging motion of a flexible rope pendulum under the influence of gravity \mathbf{g} is simulated to validate our present structure solver on solving the dynamics of a flexible object. The schematic is illustrated in Fig. 4a, where a flexible pendulum (Length $L = 1$, $N_b = 81$, $\rho_c = 1$) is pinned up at one end and is initially placed with a small angle $\theta = 0.01\text{rad}$ to the direction of gravity whose magnitude is $|\mathbf{g}| = 10$. The bending rigidity of the pendulum K_b is set to 0 in order to compare with the analytical solution. The movement of the flexible pendulum is governed by Equation (8) with the hydrodynamic force being substituted by the gravity \mathbf{g} . The analytical solution for a hanging pendulum with a small-amplitude motion can be derived using the perturbation method (Huang et al. 2007). When subject to a hinged and a free-end boundary

condition, the free-end position can be expressed in series as following

$$x(s, t) = \sum_{i=1}^{\infty} \frac{4\theta L J_2(z_i)}{z_i^2 J_1^2(z_i)} J_0\left(z_i \sqrt{\frac{L-s}{L}}\right) \cos\left(\frac{z_i}{2} \sqrt{\frac{|g|}{L}}\right) \quad (21)$$

where J_0 , J_1 and J_2 are the Bessel function of the first kind of order zero, one and two, respectively. z_i is the i th positive root of $J_0(z)$.

By using both numerical and analytical methods, the calculated free-end positions at successive time are demonstrated and compared in Fig. 4b, where a good agreement between our numerical result and the analytical result is achieved.

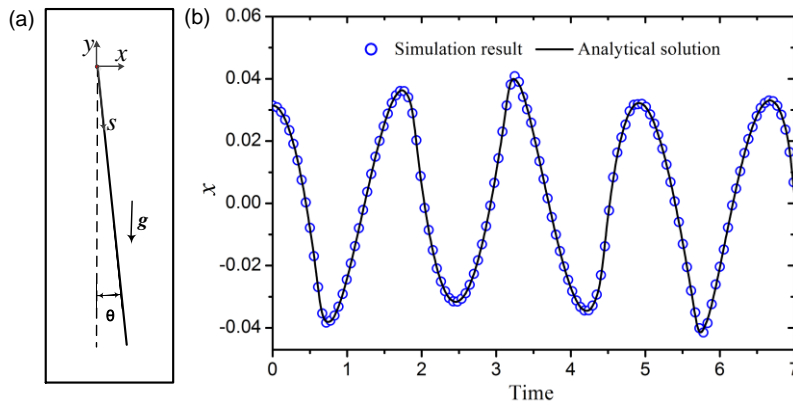


Fig. 4 Schematic view of the swinging rope pendulum (a) Comparison of the free-end positions (x -component) between numerical and analytical solutions (b)

3.3 Flow past a stationary circular cylinder

To further verify the accuracy of our coupled algorithm in solving FSI problem, a flow past a stationary circular cylinder is simulated at $Re = 20$, 40 and 100 , respectively ($Re = u_{\infty} D_c / \nu$, where u_{∞} is the velocity of the incoming flow stream, ν the viscosity of the fluid, and D_c the diameter of the cylinder which is covered with 30 Eulerian grids). The computational domain

is a square with a size of $40D_c \times 40D_c$ and the center of the cylinder is placed at $(16D_c, 20D_c)$ with its surface represented with 120 uniformly distributed Lagrangian points. The drag coefficient C_d and lift coefficient C_l are calculated using the following formulas to facilitate comparison.

$$C_d = \frac{F_d}{0.5\rho u_\infty^2 D_c}, \quad C_l = \frac{F_l}{0.5\rho u_\infty^2 D_c} \quad (22)$$

where F_d and F_l are the drag force and lift force on the surface of the cylinder, respectively.

Our calculated result is tabulated in Table 1, which agrees well with those from literature.

Table 1 Comparison of C_d , C_l with those from literature

References	Re = 20	Re = 40	Re = 100	
	C_d	C_d	C_d	C_l
Russell et al. (2003)	2.22	1.63	1.43	± 0.339
Xu et al. (2006)	2.23	1.66	1.42	± 0.34
Tian et al. (2011)	2.16	1.62	1.43	/
Yuan et al. (2014)	2.069	1.559	1.397	± 0.337
Present	2.138	1.607	1.434	± 0.347

4 Model formation and simulation setup

The model for the primary cilium dynamics is two-dimensional in the current study. Due to the large aspect ratio of the cilium (The length of endothelial primary cilia usually ranges from 1.8 to 11.1 μm , while the diameter is about 0.2 μm (Lim et al. 2015)), it is modeled as an elastic homogeneous filament with its basal end located at the centerpoint of an endothelial cell or an epithelial cell. Endothelial cells form the inner wall of blood vessels and epithelial cells form the wall of the collecting duct, which is one part of the tubule in the kidney. The dynamic motion of a cilium is governed by Equation (8). In addition, the primary cilia initially orient

perpendicularly to the wall surface and are present in a manner of periodic array in the axial (x) –direction with a spacing interval of L_d . A schematic diagram of the model geometry is shown in Fig. 5, where the rectangular area depicted by the solid line is chosen as the computational domain.

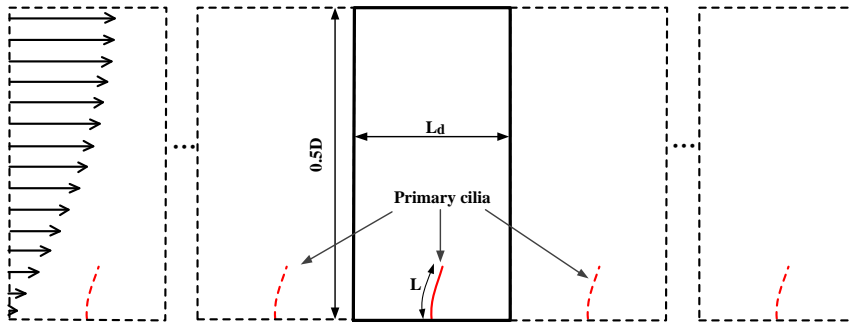


Fig. 5 Schematic view of the primary cilia periodically located at the center of endothelial cells lining the blood vessel wall

The flow is assumed to be incompressible, laminar, Newtonian and pulsatile. A body force density f_d is applied to each Eulerian point as a substitution of the pressure gradient to drive the flow. The pressure gradient waveform is plotted in Fig. 6, which is reproduced using the data of in reference (McDonald 1955). The tube wall is assumed to be rigid and impermeable. Basic parameters of the fluid-cilium coupling system in physical units are listed in Table 2. Note that typically reported values of bending rigidity for a cilium vary from 1 to $2 \times 10^{-23} \text{Nm}^2$ (Downs et al. 2014; Han et al. 2005; Schwartz et al. 1997; Young et al. 2012), so we chose an intermediate value of $1.5 \times 10^{-23} \text{Nm}^2$ in our simulations. As a result, the governing parameters of this system include cilium's structure property, the peak Reynolds number Re_{peak} , and the Womersley number Wo . The last two dimensionless numbers

characterize the flow field and are defined as

$$\text{Re}_{\text{peak}} = \frac{u_0 D}{\nu}, \quad \text{Wo} = D \sqrt{\frac{2\pi f}{\nu}} \quad (23)$$

where u_0 is the maximum flow velocity when $f = 0$, i.e. there is no oscillation. ν is the kinematic viscosity of the fluid, and f the pulsatile flow frequency.

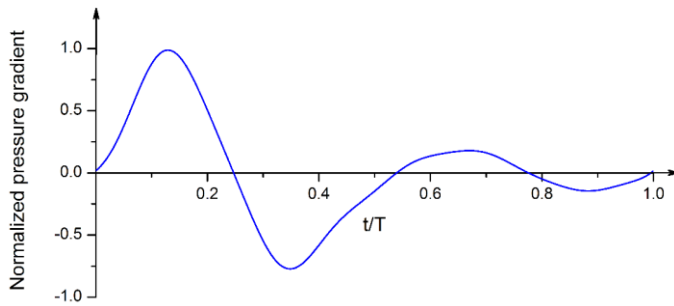


Fig. 6 The pressure gradient waveform (reproduced using the data of McDonald (1955))

Table 2 Basic parameters of the fluid-cilium coupling system in physical units

Parameter	Symbol	Physical value
Cilium length	L_c	6 μm
Cilium diameter	d_c	0.2 μm (Lim et al. 2015)
Vessel diameter	D	30 μm
Cilium spacing interval	L_d	12 μm
Fluid density	ρ_f	1000 kg/m^3
Cilium density	ρ_c	1110 kg/m^3 (Resnick 2015)
Cilium linear density	ρ_l	$4.44 \times 10^{-11} \text{kg}/\text{m}$
Fluid kinematic viscosity	ν	$1.2 \times 10^{-6} \text{m}^2/\text{s}$
Bending rigidity of cilium	K_b	$1.5 \times 10^{-23} \text{Nm}^2$
Linear spring constant	k	$4.6 \times 10^{-12} \text{N}/\text{rad}$ (Resnick 2015)
Nonlinear spring constant	α	$-1 \times 10^{-10} \text{N}/\text{rad}^2$ (Resnick 2015)
Peak Reynolds number	Re_{peak}	0.05-0.4

Boundary conditions used in our simulations are illustrated as follows:

- (1) At the inlet and outlet of the domain, a periodic boundary condition is imposed.
- (2) At the bottom wall, a bounce-back rule is imposed to satisfy no-slip boundary condition. For the upper border of the domain, a symmetry boundary condition is imposed to reduce computational cost.

- (3) For the cilium tip, a free-end boundary condition is applied, i.e. both the bending moment and transverse stress vanish at the cilium tip.

$$\frac{\partial^2 \mathbf{X}}{\partial s^2} = 0, \quad \frac{\partial^3 \mathbf{X}}{\partial s^3} = 0 \quad (24)$$

For the basal end of the cilium, as it is attached to a nonlinear rotational spring (see Fig. 2), the boundary condition becomes

$$\mathbf{X} = \mathbf{X}_0, \quad \frac{d^2 \mathbf{X}}{ds^2} - \frac{L}{K_b} \left(k \frac{d\mathbf{X}}{ds} + \alpha \left(\frac{d\mathbf{X}}{ds} \right)^2 \right) = 0, \quad \text{for } s=0 \quad (25)$$

where L is the length of the cilium, k and α the linear and nonlinear spring constants, respectively.

5 Grid convergence study

A grid convergence study is performed to ensure that the grid space we currently used is convergent and fine enough for this fluid-cilium-interaction problem. The deflection of a primary cilium under a steady flow at $Re = 0.05$ is simulated at 4 levels of grids ($\Delta x = \Delta s$ in all simulations). The time evolutions of the cilium tip position are plotted and make comparison among different grid levels in Fig. 7. It can be seen that the position is convergent as the grid get refined, and a grid size of $\Delta x \leq 1/100$ would be fine enough for this problem.

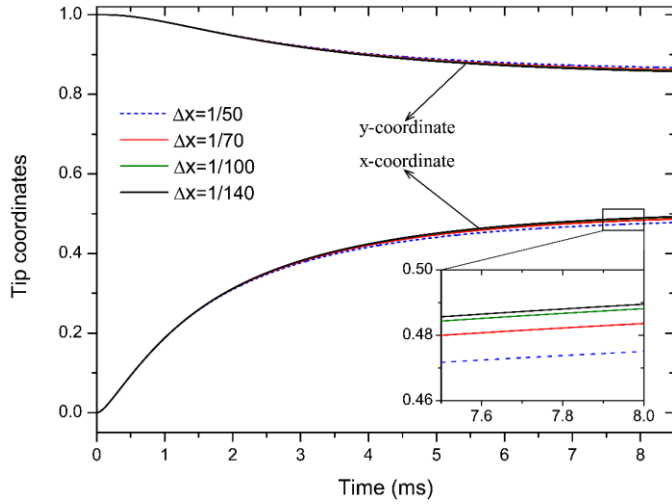


Fig. 7 Time evolutions of the tip coordinates at different grid levels

6 Results and Discussion

6.1 Effect of primary cilia on the flow field

Due to the pulsatile pressure gradient in the vessel, the flow is transient and periodic with a period T characterizing the cardiac cycle. Simulations of the flow field with and without cilia, subject to an identical flow condition ($Re_{peak}=0.2$, $Wo=0.6$), were performed. The flow fields obtained were plotted and compared in Fig. 8 with streamlines overlaid to capture the flow features. One can see that lower velocity magnitudes are generated in the near wall region and at some moments vortical flow structures are formed with a typical recirculation region found at the cilium tip due to the obstruction and deflection of the primary cilium.

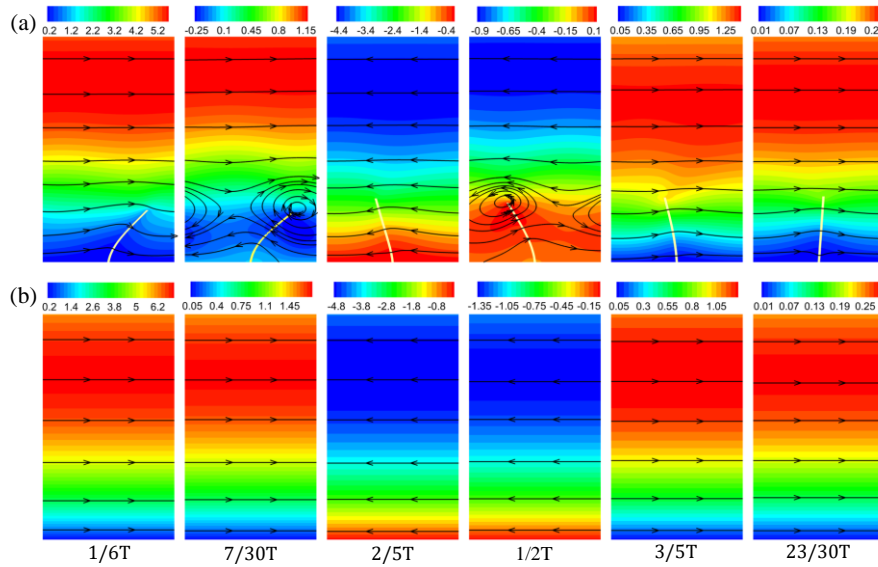


Fig. 8 Comparison of the x-velocity contour and streamlines between (a) with and (b) without cilia presented cases at six snapshots (the unit for velocity is mm/s)

The flow-induced wall shear stress (WSS) has a significant meaning in the human cardiovascular system as it is a stimulus that endothelial cells forming the vessel wall are particularly sensitive to. Both low and oscillatory WSS have been implicated as the potential causes for cardiovascular diseases such as atherosclerosis (Davies 2009). To examine the influence of the cilia on the WSS, the WSS distribution and its variation during a cardiac cycle are analyzed and compared with that of the without-cilium cases. Fig. 9 shows a comparison of WSS distributions at 9 typical moments in the presence and absence of the cilia. Both positive and negative WSS values can be observed due to the change of flow direction in each cycle as shown in Fig. 8, where reverse flows can be observed. For the case in the absence of cilia, the WSS distribution is uniform along the wall (see Fig. 9b), while for the case in the presence of cilia, the WSS distribution no longer remains uniform but varies along the wall (see Fig. 9a).

To be specific, when the cilia are present, the magnitude of the WSS fluctuates like this: at the left half region of the endothelial cell it keeps decreasing with a minimum value always found near the midpoint of the cell where a cilium is located, but at the right half region, the magnitude rises and finally stabilizes at the region near the right boundary. The WSS at 3 different sites (marked as A, B, and C in Fig. 9a) of the endothelial cell versus time is plotted in Fig. 10. One can see that the presence of cilia dramatically reduces the level of WSS at these sites, especially at the region near Site B, where the cilium is located.

Commented [CJY1]: 校稿时改过来!!!! channel

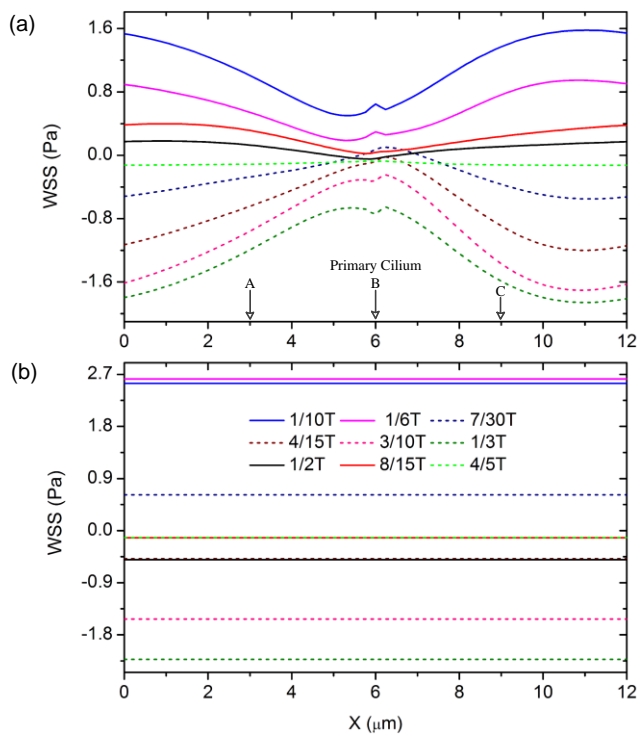


Fig. 9 Comparison of the WSS distributions at 9 moments in the presence (a) and absence (b) of the cilium

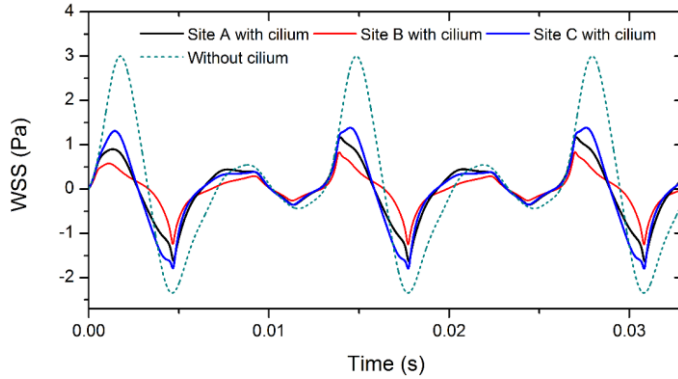


Fig. 10 Temporal fluctuation of the WSS at sites A, B, C (Fig. 11a) of the endothelial cell in the presence and absence of the cilium

6.2 Dynamics of primary cilium at various Peak Reynolds numbers

In this section, the dynamics of the cilium at various Re_{peak} , $Wo=0.6$ is studied. Our numerical results show that, after several cycles, the cilium steps into and maintains a periodic flapping pattern with its profiles and tip trajectories at different Re_{peak} shown in Fig. 11. Though a typical pressure gradient waveform in the blood vessel (Fig. 6) is adopted in our simulations to create a pulsatile flow condition, the flapping dynamics of primary cilium we observed is quite similar with the ciliary oscillation captured in renal tubular flow by O'Connor et al. (2013) using a new *in vivo* visualization tool, the Cilia^{GFP} mouse. Our simulation results support their first speculation that the oscillation behaviors of renal cilia may be due to the pulsatile flow. It is obvious and intuitive that the cilium deflection amplitude at a higher Re_{peak} is greater, as the corresponding flow drag is increased. Furthermore, for the chosen Wo of 0.6, we find that when the Re_{peak} is reduced to below a critical value, the cilium manages to flap only in the right half of the domain. This one-side flapping results in the stretch of a cilium on one side while the

other side is compressed during the entire deflection process.

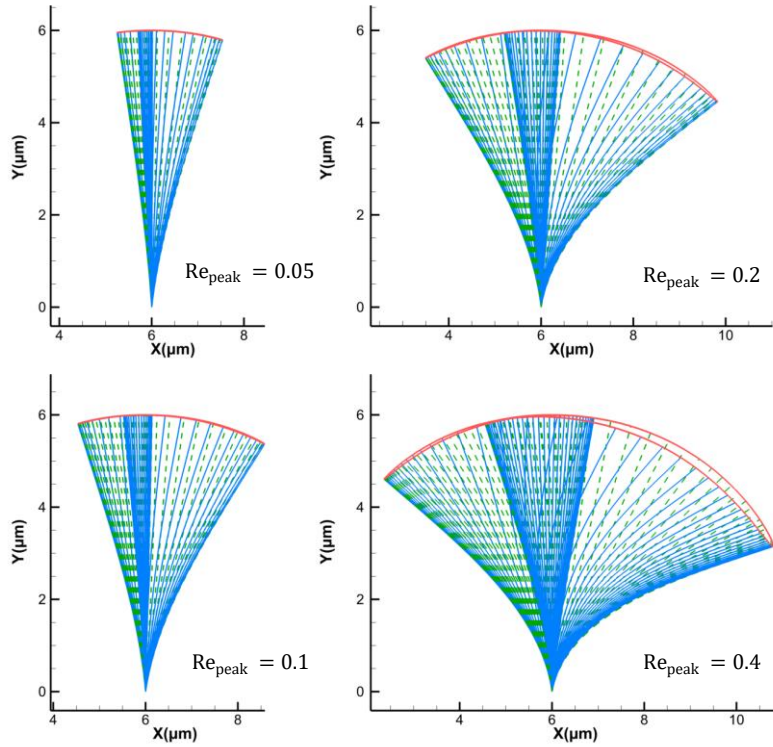


Fig. 11 The trajectories of a cilium in a cardiac cycle at various Re_{peak} with the dashed green lines indicating clockwise deflections, solid blue lines anticlockwise deflections, and solid red line tip trajectories

The angular speed of the cilium tip at various Re_{peak} is recorded and plotted in Fig. 12, where the positive and negative values denote clockwise and anticlockwise deflection, respectively. The normalized pressure gradient waveform is appended at the top of the figure to facilitate analysis. A phase lag between the angular speed and the applied pressure gradient is observed, as reported by O'Connor et al. (2016). During each cycle, the cilium is observed to first deflect clockwise at an increasing speed, then decelerate to zero before switching to an anticlockwise

deflection. It is at this zero-angular-speed moment that the cilium reaches its right deflection limit. In the subsequent anticlockwise deflection, the cilium also experiences an accelerating-decelerating “bounce-back” process before reaching its left deflection limit at the second zero-angular-speed moment. In the rest period of the cycle, the cilium repeats the aforementioned deflection behavior but at a much lower amplitude. The deflection behavior of the cilium basically follows the applied pressure gradient waveform, except that the largest angular speed value is obtained during the first anticlockwise deflection process, instead of during the first clockwise deflection, where the largest pressure gradient is applied at a positive value. This may be due to the release of the bending energy that the cilium harvested during its first clockwise deflection process, where cilium’s largest deflection and bending energy in a cycle is obtained. With the joint effect of the released bending energy and the absorbed backward flow power (due to the negative pressure gradient applied), the cilium is likely to obtain a larger kinetic energy (tip angular speed) during its anticlockwise deflection process, e.g. at time=0.0441s. As it can be further suggested from the cilium profile presented in Fig. 12, at that moment when the cilium reaches its maximum tip angular speed, the cilium has a nearly straight profile, indicating the bending energy is now at a very low level after such a release.

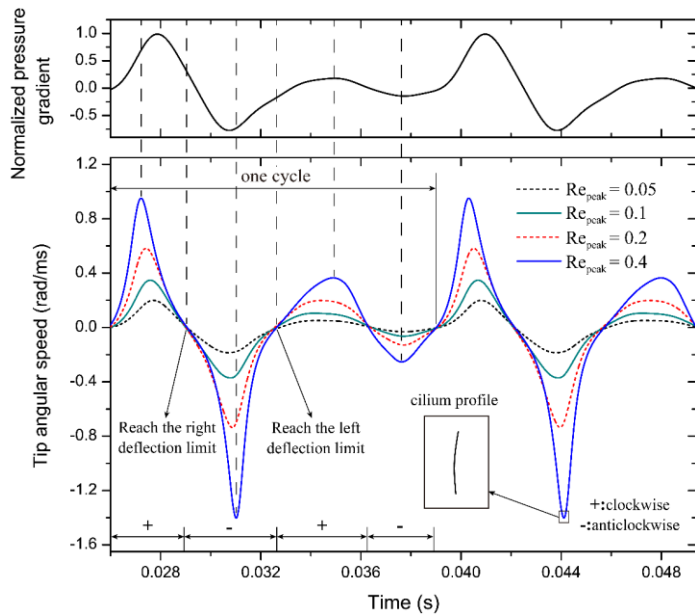


Fig. 12 Temporal fluctuation of the cilium tip angular speed at various Re_{peak} with the normalized pressure gradient waveform appended at the top for reference

Besides, the basal rotation of the cilium can be observed in all simulation cases, as shown in Fig. 13a. The variation of the maximum curvature during the deflection process is plotted in Fig. 13b. Here the maximum curvature is recorded and analyzed because experimental studies have revealed that the opening of the ion channels is correlated with the tensile stress in the cilium membrane, and the tensile stress is approximately proportional to its curvature in the primary cilium case as its large aspect ratio makes the equations derived in pure bending assumption still valid. Therefore, a larger curvature indicates a higher possibility in the activation of the stretch-sensitive ion channels during the bending process of a primary cilium and those channels localized near the point with the maximum tensile stress would get activated first. In our simulation results, due to the pulsatile flow applied, the maximum tensile stress is

not always observed at the cilium base region as reported by Rydholm et al. (2010) and Young et al (2012). According to our numerical results, the location that has the maximum tensile stress (MTS) could propagate from time to time during a cardiac cycle, though in most of time (more than 85% of a cycle in our simulated Re_{peak} cases) it stays at the base. A typical case demonstrating this phenomenon is shown in Fig. 14, where we can see that the location of the MTS periodically varies between 0 to 45% of cilium length. For all the cases we simulated, the location of MTS is observed to travel for only a certain distance from the base, and the travelled distance is more remarkable in the case with a higher Re_{peak} . From Fig. 12 and Fig. 13, one can also clearly see that when a primary cilium is subjected to a fluid flow with higher Re_{peak} , its tip angular speed, basal rotation and maximum curvature all increase.

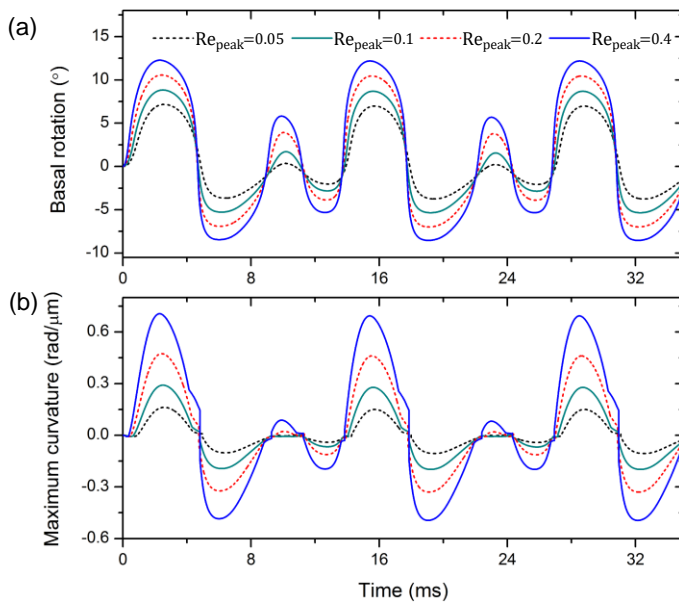


Fig. 13 Temporal fluctuation of the cilium's cilium basal rotation (a) maximum curvature (b) at various Re_{peak}

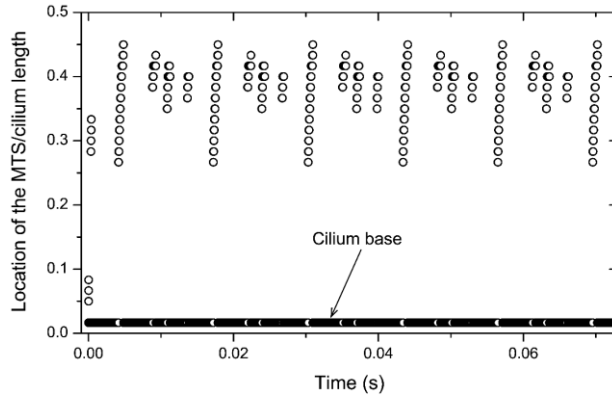


Fig. 14 Time evolution of the cilium point with the maximum tensile stress at $Re_{peak} = 0.4, Wo = 0.6$

6.3 Effect of Womersley number on the dynamics of the primary cilium

The Wo is another important dimensionless number in the cardiovascular system for characterizing the unsteady part of the flow power. In different types of human blood vessels, this number varies significantly. Based on the vessel size we chose, simulations of the deflections of the primary cilium at a certain range of Wo were also performed at $Re_{peak} = 0.1$. Varying of Wo is achieved by altering the pulsatile flow frequency f in Equation (31).

The profiles and tip trajectories of the cilium in a cardiac cycle at various Wo are presented in Fig. 15, in which we can see that as Wo increases the cilium deflection amplitude decreases. At $Wo = 1.2$, the cilium only has very few negative deflections (hereafter, the deflections occur at the left half domain ($X < 6\mu m$) are prescribed as negative deflections, otherwise positive deflections), and as Wo further increases, the cilium is unable to cross the centerline of the region, resulting in completely positive deflections, i.e. the cilium only flaps in the right

half of the domain. The reason may be that when the cilium is subject to a fluid flow with a higher Wo , the cilium could harvest less bending energy as the deflection amplitude is reduced. The release of this energy in the following “bounce-back” process is not enough to return to its initial position. The temporal fluctuations of the tip angular speed at three different Wo are displayed in Fig.16. One can see that as the Wo increases, the amplitude of the tip angular speed also increases although the deflection amplitude of the cilium decreases (see Fig. 15). However, when $Wo = 1.2$, the largest angular speed value is obtained during the first clockwise deflection process, which is quite different from the results of other cases, indicating that the release of the bending energy at this Wo is the lowest. The temporal fluctuations of the basal rotation and maximum curvature are recorded and presented in Fig. 17a and Fig. 17b, respectively. An increase in Wo results in a decrease in both quantities. This may be due to the imbalance of the portion of the applied positive and negative pressure gradient in a cardiac cycle (positive portion > negative portion, see Fig. 6). The positive portion becomes even more dominant when Wo decreases, which brings a larger average drag force to the cilium and enables it to deflect more powerfully.

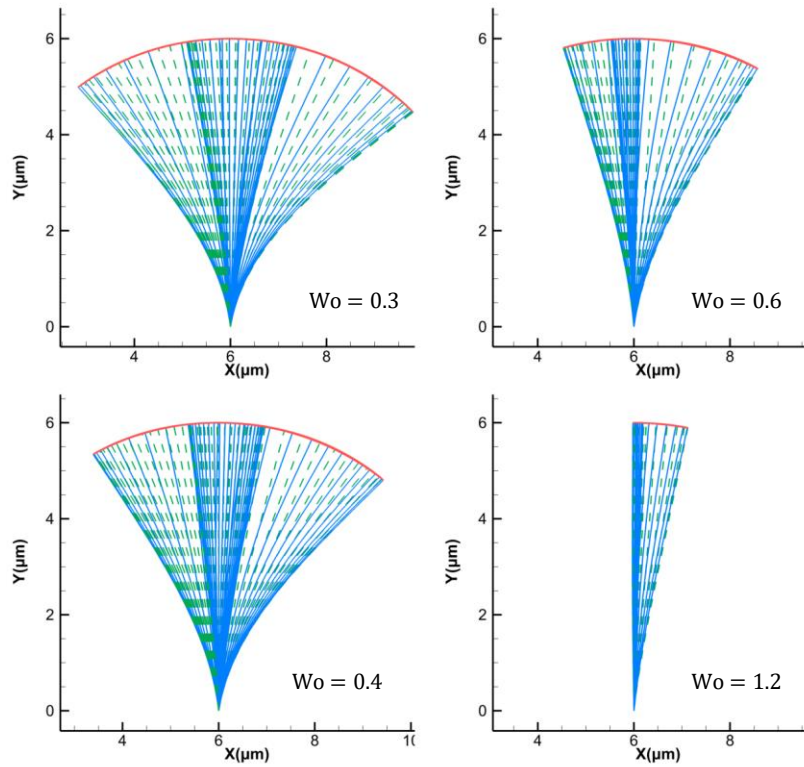


Fig. 15 The profiles of the cilium in a cardiac cycle at various Wo with the dashed green lines indicating clockwise deflections, solid blue lines anticlockwise deflections, and solid red line tip trajectories

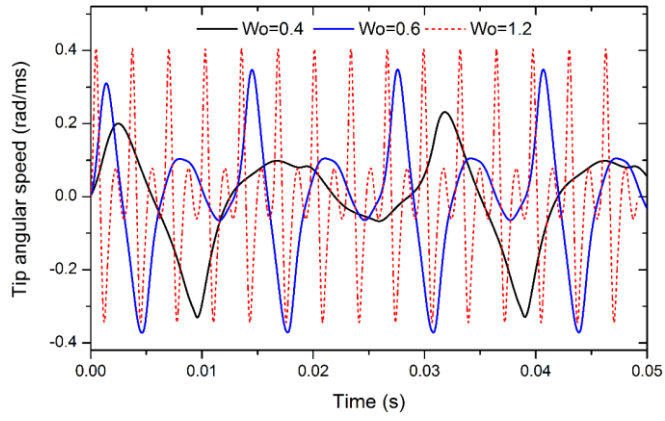


Fig. 16 Temporal fluctuation of the cilium tip angular speed at various Wo

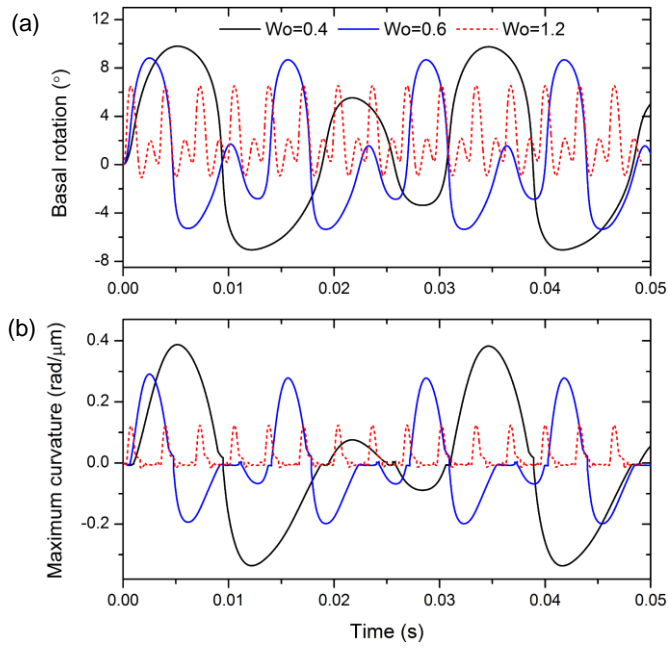


Fig. 17 Temporal fluctuation of cilium's basal rotation (a) maximum curvature (b) at various Wo

7 Conclusions

In this study, an explicit immersed boundary-lattice Boltzmann method is developed to study the dynamics of the primary cilium in pulsatile flows with two-way fluid-structure interaction taken into consideration. After validating our algorithm against several benchmark problems, the fluid-cilium interaction system is investigated in detail using our method with the cilium basal body modeled as a nonlinear rotational spring. Our simulation reproduced similar cilium flapping dynamics as those captured in the *in vivo* experiment by O'Connor et al. (2013). Based on our simulation results, some conclusions are drawn as follows:

(1). Due to the obstruction of the primary cilium, the WSS distribution no longer remains uniform as for the case without cilium but oscillates in space. The magnitude of the WSS is found to decrease at the first (left) half region of the endothelial cell with its minimum always found near the cell midpoint where the cilium is located, and the magnitude rises in the second (right) half part of the endothelial cell. The presence of the cilium also reduces the overall level of the WSS, especially at the region near the cilium anchor point.

(2). The primary cilium is observed to do a periodic flapping during each cardiac cycle. The flapping pattern depends on both the Re_{peak} and Wo . By reducing the Re_{peak} (e.g. decrease the flow rate) or enhancing the Wo (e.g. increase the pulsatile flow frequency) to a certain level, the primary cilium will switch to a one-side flapping pattern from its original two-side one, resulting in the stretch only on one side of the cilium. When a primary cilium is subject to fluid flows with higher Re_{peak} , its flapping amplitude, tip angular speed, basal rotation and maximum tensile stress all increase. In contrast, increasing the Wo reduces these four quantities.

(3). Under pulsatile flow conditions, the maximum tensile stress of the primary cilium is not always (though mostly) found at the cilium base region. In contrast, it could propagate

periodically within a certain distance to the base.

Acknowledgement Support to J.Y. Cui by PolyU RKC1 and supports given by PolyU G-UACM and G-YBG9 are gratefully acknowledged.

Reference

- Boo YC, Jo H (2003) Flow-dependent regulation of endothelial nitric oxide synthase: role of protein kinases *American Journal of Physiology-Cell Physiology* 285:C499-C508 doi:10.1152/ajpcell.00122.2003
- Connell BSH, Yue DKP (2007) Flapping dynamics of a flag in a uniform stream *J Fluid Mech* 581:33-68 doi:10.1017/s0022112007005307
- Davies PF (2009) Hemodynamic shear stress and the endothelium in cardiovascular pathophysiology *Nature clinical practice Cardiovascular medicine* 6:16-26 doi:10.1038/ncpcardio1397
- Downs ME, Nguyen AM, Herzog FA, Hoey DA, Jacobs CR (2014) An experimental and computational analysis of primary cilia deflection under fluid flow *Comput Methods Biomech Biomed Eng* 17:2-10 doi:10.1080/10255842.2011.653784
- Goetz SC, Anderson KV (2010) The primary cilium: a signalling centre during vertebrate development *Nature reviews Genetics* 11:331-344 doi:10.1038/nrg2774
- Guo Z, Zheng C, Shi B (2002) Discrete lattice effects on the forcing term in the lattice Boltzmann method *Physical Review E* 65:046308 doi:10.1103/PhysRevE.65.046308
- Hagiwara H, Ohwada N, Aoki T, Suzuki T, Takata K (2008) The primary cilia of secretory cells in the human oviduct mucosa *Med Mol Morphol* 41:193-198 doi:10.1007/s00795-008-0421-z
- Han YF, Ganatos P, Weinbaum S (2005) Transmission of steady and oscillatory fluid shear stress across epithelial and endothelial surface structures *Phys Fluids* 17:13 doi:10.1063/1.1830485
- Hanasoge S, Hesketh PJ, Alexeev A (2018) Metachronal motion of artificial magnetic cilia *Soft Matter* 14:3689-3693 doi:10.1039/c8sm00549d
- Hassounah NB, Bunch TA, McDermott KM (2012) Molecular pathways: The role of primary cilia in cancer progression and therapeutics with a focus on hedgehog signaling *Clinical Cancer Research* 18:2429-2435 doi:10.1158/1078-0432.ccr-11-0755
- Huang W-X, Shin SJ, Sung HJ (2007) Simulation of flexible filaments in a uniform flow by the immersed boundary method *Journal of Computational Physics* 226:2206-2228 doi:https://doi.org/10.1016/j.jcp.2007.07.002
- Khayyeri H, Barreto S, Lacroix D (2015) Primary cilia mechanics affects cell mechanosensation: A computational study *J Theor Biol* 379:38-46 doi:10.1016/j.jtbi.2015.04.034
- Kruger T, Holmes D, Coveney PV (2014) Deformability-based red blood cell separation in deterministic lateral displacement devices-A simulation study *Biomechanics* 8:15 doi:10.1063/1.4897913
- Ladd AJC (1994a) Numerical simulations of particulate suspensions via a discretized boltzmann-equation .1. theoretical foundation *J Fluid Mech* 271:285-309 doi:10.1017/s0022112094001771
- Ladd AJC (1994b) Numerical simulations of particulate suspensions via a discretized boltzmann-equation .2. numerical results *J Fluid Mech* 271:311-339 doi:10.1017/s0022112094001783
- Lim YC, McGlashan SR, Cooling MT, Long DS (2015) Culture and detection of primary cilia in endothelial

- cell models *Cilia* 4:11 doi:10.1186/s13630-015-0020-2
- Liu W, Murcia NS, Duan Y, Weinbaum S, Yoder BK, Schwiebert E, Satlin LM (2005) Mechanoregulation of intracellular Ca²⁺ concentration is attenuated in collecting duct of monocilium-impaired orpk mice *American journal of physiology Renal physiology* 289:F978 doi:10.1152/ajprenal.00260.2004
- Masyuk AI, Masyuk TV, LaRusso NF (2008) Cholangiocyte primary cilia in liver health and disease *Developmental Dynamics* 237:2007-2012 doi:10.1002/dvdy.21530
- McDonald DA (1955) The relation of pulsatile pressure to flow in arteries *The Journal of physiology* 127:533 doi:10.1113/jphysiol.1955.sp005275
- McGlashan SR, Cluett EC, Jensen CG, Poole CA (2008) Primary cilia in osteoarthritic chondrocytes: From chondrons to clusters *Developmental Dynamics* 237:2013-2020 doi:10.1002/dvdy.21501
- Menzl I et al. (2014) Loss of primary cilia occurs early in breast cancer development *Cilia* 3:7 doi:10.1186/2046-2530-3-7
- Nauli SM et al. (2003) Polycystins 1 and 2 mediate mechanosensation in the primary cilium of kidney cells *Nature Genet* 33:129-137 doi:10.1038/ng1076
- Nauli SM, Kawanabe Y, Kaminski JJ, Pearce WJ, Ingber DE, Zhou J (2008) Endothelial cilia are fluid shear sensors that regulate calcium signaling and nitric oxide production through polycystin-1 *Circulation* 117:1161-1171 doi:10.1161/circulationaha.107.710111
- Nguyen AM, Jacobs CR (2013) Emerging role of primary cilia as mechanosensors in osteocytes *Bone* 54:196-204 doi:10.1016/j.bone.2012.11.016
- Nguyen AM, Young YN, Jacobs CR (2015) The primary cilium is a self-adaptable, integrating nexus for mechanical stimuli and cellular signaling *Biol Open* 4:1733-1738 doi:10.1242/bio.014787
- Niu XD, Shu C, Chew YT, Peng Y (2006) A momentum exchange-based immersed boundary-lattice Boltzmann method for simulating incompressible viscous flows *Phys Lett A* 354:173-182 doi:10.1016/j.physleta.2006.01.060
- O'Connor J, Revell A, Mandal P, Day P (2016) Application of a lattice Boltzmann-immersed boundary method for fluid-filament dynamics and flow sensing *J Biomech* 49:2143-2151 doi:10.1016/j.jbiomech.2015.11.057
- O'Connor J, Revell A, Mandal P, Day P (2016) Application of a lattice Boltzmann-immersed boundary method for fluid-filament dynamics and flow sensing *Journal of Biomechanics* 49:2143-2151 doi:10.1016/j.jbiomech.2015.11.057
- O'Connor AK et al. (2013) An inducible Cilia^{GFP} mouse model for in vivo visualization and analysis of cilia in live tissue *Cilia* 2:8 doi:10.1186/2046-2530-2-8
- Peskin CS (2003) The immersed boundary method *Acta Numerica* 11:479-517 doi:10.1017/S0962492902000077
- Praetorius HA, Frokiaer J, Nielsen S, Spring KR (2003) Bending the primary cilium opens Ca²⁺-sensitive intermediate-conductance K⁺ channels in MDCK cells *J Membr Biol* 191:193-200 doi:10.1007/s00232-002-1055-z
- Praetorius HA, Spring KR (2001) Bending the mdck cell primary cilium increases intracellular calcium *The Journal of Membrane Biology* 184:71-79 doi:10.1007/s00232-001-0075-4
- Praetorius HA, Spring KR (2003) Removal of the MDCK Cell Primary Cilium Abolishes Flow Sensing *The Journal of Membrane Biology* 191:69-76 doi:10.1007/s00232-002-1042-4
- Resnick A (2015) Mechanical properties of a primary cilium as measured by resonant oscillation *Biophys J* 109:18-25 doi:10.1016/j.bpj.2015.05.031

- Resnick A (2016) HIF stabilization weakens primary cilia PLoS One 11:15 doi:10.1371/journal.pone.0165907
- Russell D, Jane Wang Z (2003) A cartesian grid method for modeling multiple moving objects in 2D incompressible viscous flow Journal of Computational Physics 191:177-205 doi:https://doi.org/10.1016/S0021-9991(03)00310-3
- Rydholm S, Zwartz G, Kowalewski J, Kamali-Zare P, Frisk T, Brismart H (2010) Mechanical properties of primary cilia regulate the response to fluid flow American Journal of Physiology 298:F1096 doi:10.1152/ajprenal.00657.2009
- Schwartz EA, Leonard ML, Bizios R, Bowser SS (1997) Analysis and modeling of the primary cilium bending response to fluid shear Am J Physiol-Renal Physiol 272:F132-F138
- Sen Gupta P, Prodromou NV, Chapple JP (2009) Can faulty antennae increase adiposity? The link between cilia proteins and obesity J Endocrinol 203:327-336 doi:10.1677/joe-09-0116
- Tian F-B, Luo H, Zhu L, Liao JC, Lu X-Y (2011) An efficient immersed boundary-lattice Boltzmann method for the hydrodynamic interaction of elastic filaments Journal of Computational Physics 230:7266-7283 doi:https://doi.org/10.1016/j.jcp.2011.05.028
- Xu S, Wang ZJ (2006) An immersed interface method for simulating the interaction of a fluid with moving boundaries Journal of Computational Physics 216:454-493 doi:https://doi.org/10.1016/j.jcp.2005.12.016
- Yoder BK (2007) Role of primary cilia in the pathogenesis of polycystic kidney disease J Am Soc Nephrol 18:1381-1388 doi:10.1681/asn.2006111215
- Yoder BK, Hou XY, Guay-Woodford LM (2002) The polycystic kidney disease proteins, polycystin-1, polycystin-2, polaris, and cystin, are co-localized in renal cilia J Am Soc Nephrol 13:2508-2516 doi:10.1097/01.asn.0000029587.47950.25
- Young YN, Downs M, Jacobs CR (2012) Dynamics of the Primary Cilium in Shear Flow Biophys J 103:629-639 doi:10.1016/j.bpj.2012.07.009
- Yuan HZ, Niu XD, Shu S, Li MJ, Yamaguchi H (2014) A momentum exchange-based immersed boundary-lattice Boltzmann method for simulating a flexible filament in an incompressible flow Comput Math Appl 67:1039-1056 doi:10.1016/j.camwa.2014.01.006
- Zhu LD, Peskin CS (2003) Interaction of two flapping filaments in a flowing soap film Phys Fluids 15:1954-1960 doi:10.1063/1.1582476